IMAGING METHODOLOGY – Full Papers

Magnetic Resonance in Medicine 76:417–429 (2016)

Pseudo-Projection–Driven, Self-Gated Cardiac Cine Imaging Using Cartesian Golden Step Phase Encoding

Liheng Guo,[1] J. Andrew Derbyshire,[2] and Daniel A. Herzka[1]*

Purpose: To develop and evaluate a novel two-dimensional self-gated imaging technique for free-breathing cardiac cine MRI that is free of motion-detection overhead and requires minimal planning for motion tracking.

Methods: Motion along the readout direction was extracted solely from normal Cartesian imaging readouts near $k_y = 0$. During imaging, the readouts below a certain $|k_y|$ threshold were scaled in magnitude and filtered in time to form "pseudo-projections," enabling projection-based motion tracking along readout without frequently acquiring the central phase encode. A discrete golden step phase encode scheme allowed the $|k_y|$ threshold to be freely set after the scan while maintaining uniform motion sampling.

Results: The pseudo-projections stream displayed sufficient spatiotemporal resolution for both cardiac and respiratory tracking, allowing retrospective reconstruction of free-breathing non-electrocardiogram (ECG) cines. The technique was tested on healthy subjects, and the resultant image quality, measured by blood-myocardium boundary sharpness, myocardial mass, and single-slice ejection fraction was found to be comparable to standard breath-hold ECG-gated cines.

Conclusion: The use of pseudo-projections for motion tracking was found feasible for cardiorespiratory self-gated imaging. Despite some sensitivity to flow and eddy currents, the simplicity of acquisition makes the proposed technique a valuable tool for self-gated cardiac imaging. **Magn Reson Med 76:417–429, 2016.**

Key words: golden step; self-navigation; self-gating; respiratory motion; motion tracking; pseudo-projections; cardiac imaging

INTRODUCTION

Cardiac cine MRI is an important clinical tool that visualizes the anatomy and function of a beating heart (1). Speed of data acquisition is critical to achieve sufficient spatiotemporal resolutions. However, imaging speed is almost always restricted by MR gradient hardware or risk of peripheral nerve stimulation. The amount of k-space data required for diagnostically meaningful resolutions is often too large to be acquired in real time [eg, (2–4)]. Thus, k-space data are acquired in segments during multiple cycles of cardiac motion, which are assumed to be periodic. Subsequently, imaging data are sorted retrospectively according to their temporal phase in the motion cycle to reconstitute a high-resolution cine.

When motion is monitored using MRI data itself, the acquisition is "self-gated." Numerous self-gated techniques have been developed, with diverse overhead impinging on data acquisition. Intensity tracking of the k-space origin was originally developed for cardiac self-gated imaging to replace electrocardiogram (ECG) gating and to avoid ECG-related problems such as detection error (5,6) and safety concerns (7,8). The magnitude of the k-space center is filtered and is considered a waveform that represents cardiac motion. The k-space origin can be easily acquired at high temporal resolution such as every repetition time (TR) with little or no acquisition overhead in both Cartesian (9,10) and radial trajectories (11–13). However, because the k-space origin represents the summation of the entire imaging slice or volume, successful tracking of cardiac motion requires the total blood signal to vary significantly over time according to cardiac rhythm, which may not be the case if the heart's pumping function is impaired (9), or if the heart chambers show out-of-phase contractions that superimpose destructively (12). Similarly, using the k-space origin to track the more challenging respiratory motion is reliable only under certain restrictions (10,12).

The k-space origin can provide the highest temporal resolution albeit with a lack of spatial discrimination within the imaging volume due to the summation. Conversely, low-resolution image-based techniques can measure more information at reduced temporal resolution. For example, a small number of radial k-space readouts acquired periodically and reconstructed to low-resolution images can detect motion (11,14,15). Alternatively, the PROPELLER method reconstructs the low-resolution images from a small number of parallel low-k_y Cartesian readouts (16,17). Most low-resolution image-based methods require radial trajectories, which are more challenging to implement and to reconstruct than Cartesian

[1]Department of Biomedical Engineering, Johns Hopkins University School of Medicine, Baltimore, Maryland, USA.

[2]Functional MRI Facility, National Institute of Mental Health, National Institutes of Health, Bethesda, Maryland, USA.

*Correspondence to: Daniel A. Herzka, PhD, Department of Biomedical Engineering, Johns Hopkins University School of Medicine, 720 Rutland Avenue, Suite 726, Ross Building, Baltimore, MD 21205. E-mail: daniel.herzka@jhu.edu

Received 29 January 2015; revised 17 May 2015; accepted 15 June 2015

DOI 10.1002/mrm.25834

Published online 31 October 2015 in Wiley Online Library (wileyonlinelibrary.com).

trajectories due to gradient delay errors that affect the k-space trajectory and require additional correction.

Projection-based motion tracking provides more information than k-space origin tracking and has higher temporal resolution than image-based tracking. The projection-slice theorem states that the inverse Fourier transform of a readout line that traverses the center of k-space is the projection of the slice. If such readouts are acquired periodically, one can extract motion from the stream of resultant projections, known as navigator projections. In radial sequences, all the readouts are themselves navigator projections, resulting in cost-free and high-frequency projection-based motion tracking (11,18). In Cartesian sequences, the navigator projections can also be acquired in every TR if they are interleaved with imaging readouts, but incurring acquisition overhead and loss of imaging efficiency (19–23). As a compromise, the Cartesian central phase encode (PE) at $k_y = 0$ can be acquired at a slower rate to measure motion, but normal imaging acquisition must be interrupted at a predetermined interval to traverse $k_y = 0$ (24–27).

Cartesian readouts at near-center PE positions, although not projections per se, can be used to measure motion. One can detect and correct rigid-body motion using such readouts (28–30) and also detect non-rigid motion (31) and regenerate corrupt data (30). However, these techniques have only targeted static image acquisition.

In a previous study, we proposed a Cartesian acquisition technique that used near-center imaging readouts to track motion and guide retrospective cine reconstruction (32). It required no dedicated navigator readout and was therefore free of loss in imaging efficiency. Furthermore, it used golden step PE ordering to allow retrospectively adjustable motion sampling rate. The golden angle technique was originally proposed to enable flexible inclusion of radial readouts for image reconstruction (33). In our present study, it enabled flexible inclusion of Cartesian imaging readouts as motion measurements while maintaining uniform sampling in time. We demonstrate the ability of the near-center Cartesian readouts to reveal motion at high spatiotemporal resolution and to guide the reconstruction of cardiac cines without ECG or breathing holding. We evaluate the resultant image quality in terms of image sharpness and functional measurements.

THEORY

In this section, we show mathematically how a two-dimensional (2D) object projects onto a stream of near-center Cartesian readouts to reveal its x motion and present the golden step scheme and its theoretical benefits.

Motion Detection Using Near-Center Readouts

In this study, the interval centered on $k_y = 0$ within which the Cartesian readouts are considered "near center" and used for motion tracking will be referred to as the "navigator zone." For a 2D object $f(x,y)$, the x inverse Fourier transform of the central phase encode is its projection along the x axis and can be written as

$$p(x) = \int f(x,y)e^{-j2\pi y k_y}\,dy|_{k_y=0} = \int f(x,y)dy. \quad [1]$$

Because $f(x - \Delta x, y)$ would yield $p(x-\Delta x)$, translational motion of the object along x is preserved in its projection. Existing motion-tracking algorithms (24,34,35) can readily process $p(x-\Delta x(t))$ to extract the displacement Δx throughout time.

In this study, we define the "pseudo-projection" as the magnitude of the x inverse Fourier transform of a noncentral phase encode, which can be written as

$$A(x,k_y) = \left|\int f(x,y)\mathrm{e}^{-j2\pi y k_y}\,dy\right|. \quad [2]$$

Because only magnitude information is taken, any object displacement (assuming rigid motion) along the y direction is not reflected on its pseudo-projection:

$$\begin{aligned} A'(x,k_y) &= \left|\int f(x,y-\Delta y)\mathrm{e}^{-j2\pi y k_y}\,dy\right| \\ &= \left|\left(\int f(x,y)\mathrm{e}^{-j2\pi y k_y}\,dy\right)\mathrm{e}^{-j2\pi\Delta y k_y}\right| \\ &= A(x,k_y) \end{aligned} \quad [3]$$

A key assumption of this study is that the pseudo-projection at a higher k_y can be related to the magnitude of the central projection at $k_y = 0$ with

$$A(x,k_y) = c(x,k_y)A(x,k_y=0), \quad [4]$$

where the magnitude scaling factor $c(x, k_y)$ is dependent on the particular slice imaged and can be obtained from fully sampled x-k_y domain data.

Ideally, a separate magnitude scaling factor $c(x, k_y)$ needs to be found for each motion state. Because motion is unknown, the x variation of $c(x, k_y)$ is assumed to be small enough such that a single $c(x, k_y)$ can be used for all states of x-motion. For a motion scan, $c(x, k_y)$ can be determined from the average of all data acquired, which is the average of all motion states. Thus for any displacement Δx, we assume

$$A(x-\Delta x,k_y) = c(x,k_y)A(x-\Delta x,\ k_y=0). \quad [5]$$

In other words, we approximate the true projection using the k_y- and x-dependent scaling of a noncentral pseudo-projection. The above expression is meaningful only to a limited extent of $|k_y|$, because at large $|k_y|$, $A(x, k_y)$ diminishes toward noise level and the calculation of $c(x, k_y)$ becomes unreliable.

Golden-Step Phase Encode Ordering

We used a discrete variation of the Cartesian golden step (36) PE ordering: in a k_y grid comprised of F_N phase encodes, where a PE index of 0 represents the most negative k_y, the PE index is advanced by F_{N-1} lines after every readout. F_{N-1} and F_N are two consecutive Fibonacci numbers (eg, $F_{11} = 89$, $F_{12} = 144$), whose ratio approximates the golden ratio $(1+\sqrt{5})/2 \approx 1.61$. If the PE index exceeds F_N, the modulo operator is applied—that is, the nth PE index is ($n\ F_{N-1}$) mod F_N. Note that all the PEs in k-space are acquired exactly once every F_N readouts.

Also, as a result of golden step PE ordering, the readout placement within any subsection of k_y-space is approximately uniform in time and in k_y (Fig. 1). Thus, the extent of k-space that makes up the navigator zone can be freely and retrospectively adjusted to attain desired motion-tracking

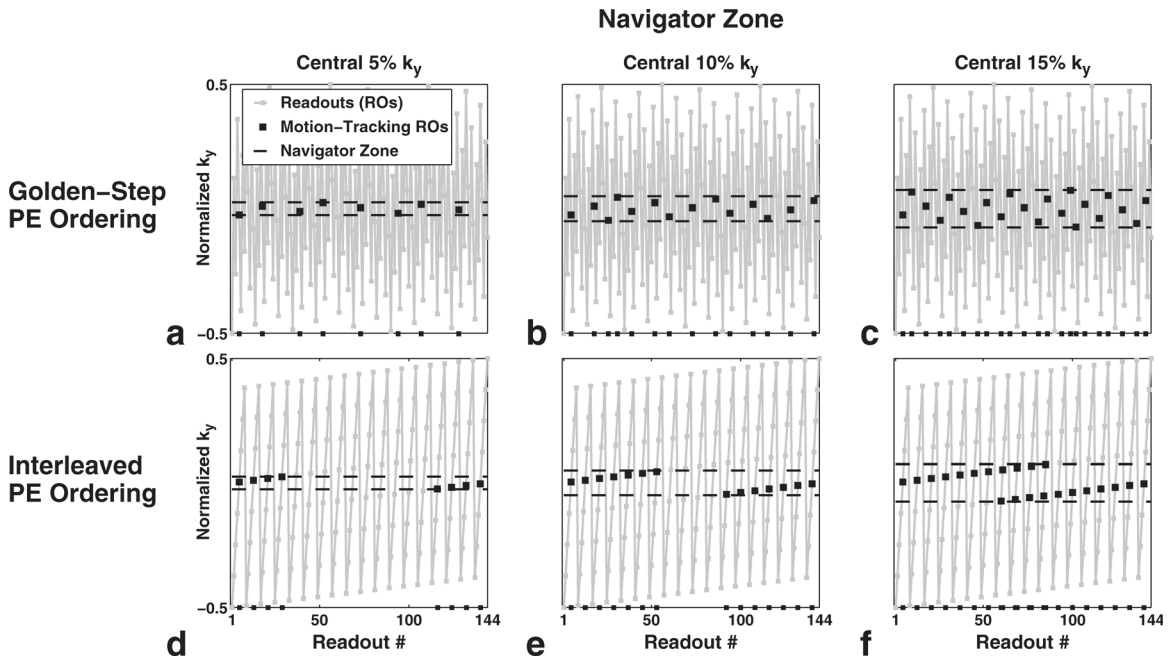

FIG. 1. (a–**c**) Discrete golden-step PE ordering. A Cartesian k_y grid with 144 evenly spaced PEs is covered exactly once by incrementing the PE index by 89 after each readout, where 89 and 144 are consecutive Fibonacci numbers. A central subsection of k_y is used as the "navigator zone" (dashed lines), within which the imaging readouts are used for motion tracking. The golden step PE ordering allows for approximately uniform coverage in time and in k_y at any navigator zone width, shown here varying from 5% to 15%. (**d–f**) In comparison, another commonly used PE ordering, the interleaved ordering, cannot maintain uniformity because it shows large gaps in coverage in certain navigator-zone widths (**d** and **e**). A total of 144 PEs and eight readouts per segment are shown.

temporal resolution while maintaining the near-uniform coverage (Figs. 1a–c). If $1/q$ of the full extent of k_y is used as the navigator zone, the average temporal resolution of motion measurement is qTR, where TR is the repetition time. For comparison, interleaved PE ordering, a widely used PE ordering scheme, would not be able to provide approximately uniform temporal resolution in the coverage of the navigator zone, because large temporal gaps may exist depending on navigator-zone widths, as shown in Figure 1d–1f. Thus in a golden step scan, one would simply continuously and repeatedly cover the F_N readouts until enough data are accumulated. The scan can be terminated at any time without losing uniformity in k_y coverage while retaining flexibility in the selection of navigator zone size.

METHODS

Simulations

To visualize object motion as seen on pseudo-projections, several moving circular phantoms were simulated using MATLAB (MathWorks, Natick, Massachusetts, USA), and their pseudo-projections at various phase encode positions were generated. In separate discrete time simulations, phantoms with diameters of 1/2, 1/4, 1/8, and 1/16 field of view (FOV) representing solid objects of increasing sizes were displaced around the center of the FOV along the x axis (Fig. 2). Pseudo-projections at 0, 1, 2, 4, 8, and 16 $\times$ Δk_y were generated.

Sequence

A Cartesian balanced steady state free precession (bSSFP) sequence was implemented to perform discrete golden step phase encoding. Gradient waveforms were designed using hardware-optimized trapezoids (37), which minimized the k-space transition times between slice selection and readouts and vice versa: for any user-defined slice orientation, gradients were customized so that during the transitions at least one gradient axis reached the limit of amplitude or slew rate.

Imaging Experiments

With local Institutional Review Board approval and after obtaining informed consent, eight healthy subjects (men, n = 3; women, n = 5; mean age, 29 ± 6 y) were imaged using a 1.5T clinical system (Avanto; Siemens Medical Solutions, Erlangen, Germany). The standard chest phased array and spine coils were used to provide a total of five channels, and data were saved separately for each channel. All scans were initiated with a half–flip angle, half–TR opening sequence (38) followed by 100 dummy TRs to transition into steady state. All scans were acquired with a matrix size of 192 $\times$ 144 (F_{12}) and a 300 $\times$ 225 mm^2 FOV, resulting in 1.56 $\times$ 1.56 mm^2 in-plane resolution. Other imaging parameters were: slice thickness = 10 mm, flip angle = 45°, and bandwidth = 650 Hz/pixel. With the optimized gradients, TR ranged from 2.5 to 2.7 ms in all scans, and the echo time was TR/2.

For each subject, a midventricular short axis (SAX) slice and a four-chamber long axis (LAX) slice were imaged. For each slice, three scans were performed. First, a breath-held, prospectively ECG-gated segmented cine (ECG BH) was acquired as the gold standard for image quality. Each segment consisted of 12 readouts, resulting in temporal resolutions of 30∼33 ms (without view sharing) and 12-heartbeat

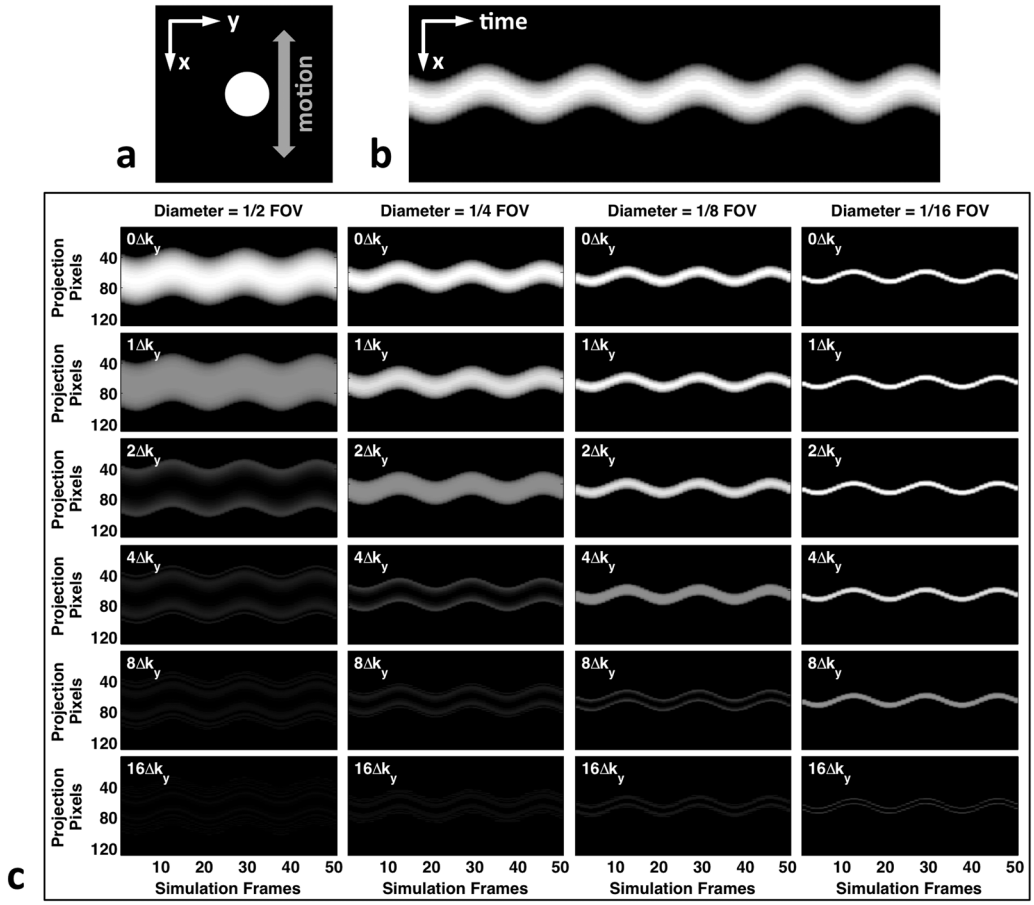

FIG. 2. Pseudo-projections of 2D solid circular phantoms (**a**) with diameters of 1/2, 1/4, 1/8, and 1/16 FOV were simulated to undergo sinusoidal motion (**b**). Their *x* inverse Fourier transforms of readouts at 0, 1, 2, 4, 8, and 16 $\times$ Δk_y phase encodes were generated (**c**). Smaller phantoms were found to retain projection appearance until higher phase encodes compared with larger phantoms, because the Fourier transform of narrower objects are more spread out in k-space.

breath-holds. The segments were acquired sequentially from negative to positive k_y. Then, the same 144 phase-encode positions were covered using discrete golden step continuously and repeatedly without ECG gating over a 12-s breath-hold to assess cardiac motion tracking alone (GS BH). To assess respiratory motion tracking, a free-breathing golden step scan (GS FB) was acquired for 90 s, representing approximately 240 complete acquisitions of k-space. The ECG-derived cardiac triggers were recorded during both golden step scans as the timing reference.

Postprocessing

In summary, cardiac motion and respiratory motion were separately extracted from the pseudo-projections to guide cardiac and respiratory self-gating, followed by similarity-based data sorting to further improve accuracy.

Cardiac self-gating was applied to both GS BH and GS FB scans, whereas respiratory self-gating was applied only to the latter. Their image quality was quantitatively compared with that of the ECG BH scans.

Pseudo-Projection Stream Formation

As shown in Figure 3, imaging readouts within the navigator zone were concatenated in time to form the stream of pseudo-projections. Wider navigator zones included more imaging readouts for motion tracking, resulting in a higher sampling rate of motion. However, the additional pseudo-projections from higher k_y had lower signal level. In this study, 10% of k_y space centered around $k_y = 0$ was chosen, because $1/q = 10\%$ provided an empirical balance of a motion-measurement interval of $10 \cdot \mathrm{TR}$ (equivalent to $\sim$38 Hz) and a tolerable pseudo-projection signal drop-off (to about $20\% \pm 5\%$ of the signal magnitude at $k_y = 0$ across all subjects).

The stream of pseudo-projections exhibited significant k_y-dependent intensity fluctuation over time, which was normalized using the scaling factor $c(x, k_y)$ (Eq. 4). The scaling factor for each coil, sized F_N by N_x (N_x being the number of points in a readout), was found by averaging all acquired navigator-zone readouts at each k_y, taking the inverse Fourier transform along readout, and normalizing the resultant magnitude with that of $k_y = 0$:

$$c(x, k_y) = \frac{\left|\sum_{i \in M} s_{i,ky}(x)\right|}{\left|\sum_{i \in M} s_{i,ky=0}(x)\right|}, \qquad [6]$$

where $s_{i,ky}$ is the readout at k_y during the ith repetition of k-space coverage and M is the total number of

repetitions in the scan. Motion was disregarded during the averaging process, and one $c(x, k_y)$ was used for all motion states.

To further reduce k_y-dependent intensity fluctuation in the pseudo-projections, the stream was smoothed along time dimension with a Gaussian window, whose full width at half maximum was F_N/q points. The aim of the smoothing step was to reduce the risk of any residual intensity fluctuation being detected as a significant motion component.

Cardiac Motion Tracking

The goal of this step was to extract from the pseudo-projection stream a one-dimensional waveform in time that would describe the motion of the heart, from which cardiac triggers would be derived to replace the ECG.

First, a simple method based on principal component analysis (PCA) was used to extract the cardiac waveform (39): the five largest eigenvalues and their corresponding eigenvectors were computed for the pseudo-projections covariance matrix $\mathbf{AA^T}$. The matrix $\mathbf{A}$ of size $N_{TR} \times (N_x * N_c)$ consisted of N_{TR} pseudo-projections acquired throughout the scan (N_x pixels per projection, N_c coils concatenated along the column dimension). The five eigenvectors were each Fourier-transformed in time, and the strongest frequency on any eigenvector between 40 and 90 beats per minute was detected as the cardiac frequency. The latter value was used because it corresponded well with the heart rates of healthy subjects, though higher values could also be used for patients with faster cardiac rhythm. The eigenvector with the most energy at this frequency was used as the cardiac waveform.

Subsequently, the waveform was filtered by a band-pass filter (lower and upper cutoff frequencies at $0.5\times$ and $2\times$ that of the detected cardiac frequency) before being passed to a moving-average-crossing (MAC) algorithm (40), with a moving average window width twice the mean duration of detected cardiac cycles. For each waveform cycle, the algorithm generated four events: peak, trough, up crossing, and down crossing. For each scan, the event type with the lowest variance in event intervals was selected to provide cardiac triggers, although any event type could be used.

To quantitatively evaluate the accuracy of cardiac self-gating, the timing error of self-gating events with respect to the ECG-derived triggers was calculated for each type of event: 1) the timing lag of every self-gating event with respect to its corresponding ECG trigger was found; and 2) the standard deviation of all time lags was calculated and considered the timing error for the scan. This was repeated for all event types and all golden step scans. The mean of the time lags was not used because the cardiac waveform, an eigenvector, might have arbitrary phase lag with respect to signal intensity or anatomical motion. Also, as a result, the cine frames were shifted after reconstruction to match the start point of the reference cine.

The intervals between pairs of consecutive events were divided into N_{cp}-many cardiac phases using a model that scales systolic and diastolic phases separately according to cardiac cycle lengths (41). For each golden step scan, N_{cp} was chosen such that the resultant average temporal resolution matched that of its reference scan. Cardiac cycles whose length differed from the mean of the scan by more than $\pm 30\%$ were considered irregular and were discarded.

Respiratory Motion Tracking

Respiratory waveform extraction and filtering was similar to that described in the previous section, though with a frequency selection range of 4–30 cycles per minute. For respiratory gating, the most frequently occurring value of the respiratory waveform was first identified [presumably at end-expiration, where respiratory motion dwells the longest (42)]. A window was then chosen around this value (symmetrically if possible) so that 30% of the time the waveform coursed within this window. Imaging readouts acquired when the waveform was within the window were used in the next stage of processing. Given the single respiratory bin, readouts were assigned to N_{cp}-many cardiorespiratory bins resulting in a cine with N_{cp} phases.

Similarity-Based Data Sorting

To reduce potential errors due to the periodicity-repeatability assumption in gating, readouts admitted to each bin were further selected for consistency. First, for each cardiorespiratory bin, the mean of all admitted processed pseudo-projections was found and regarded as the template pseudo-projection for that bin. Second, readouts admitted to the bin were ranked by their corresponding processed pseudo-projections' similarity to the template in the sum-square-difference sense. Third, for each k_y position in the bin, only the most similar readout (or top two most similar readouts in free-breathing scans with abundant data) was used in image reconstruction. If no readout was available at a particular phase k_y position in a cardiorespiratory bin, cardiac gating was relaxed to include readouts from the two adjacent cardiac phases, after which the same template-based selection was applied.

To enable such similarity-based matching, every readout needed a corresponding projection in the pseudo-projection stream. The stream had a temporal resolution of qTR and was thus linearly interpolated in time to a temporal resolution of 1 TR.

The final selection of readouts was reconstructed separately for each coil using inverse Fourier transform and combined via root-sum-squares. Parallel imaging or iterative reconstruction techniques were not used because they might affect image quality and confound the results of motion tracking.

Image Quality Evaluation

To measure image sharpness, three profiles were manually drawn across the left-ventricular (LV) blood-myocardium boundary. They were drawn on the septal wall to avoid the papillary muscles and trabeculae carnae. Along each profile, the distance (in fractional pixels) it took for the image intensity to rise from 20% to 80% of profile dynamic range was found, and the

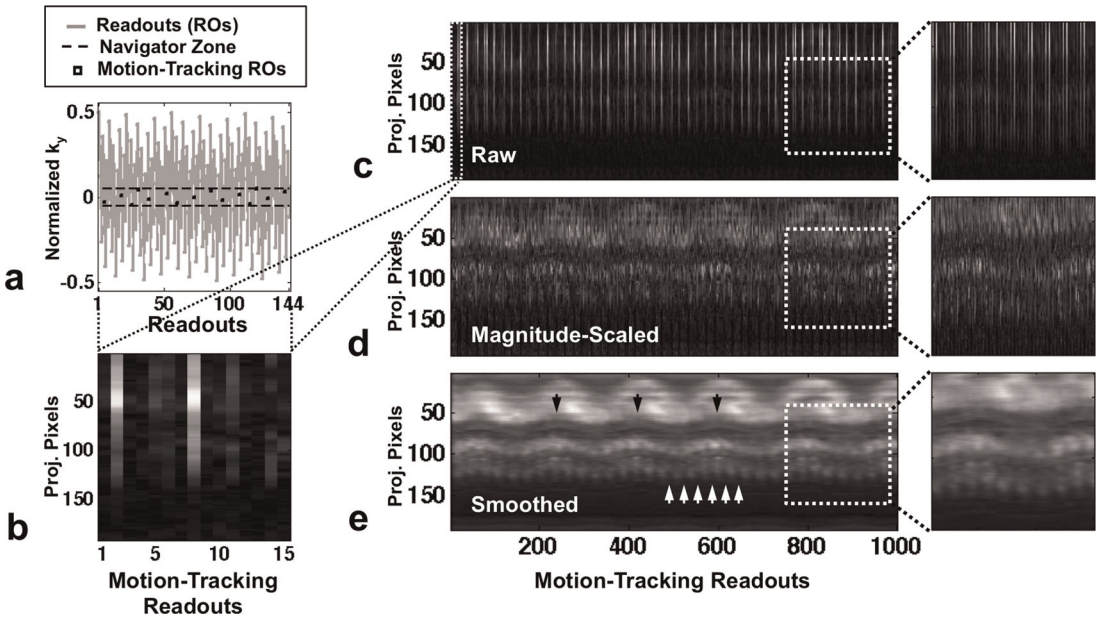

FIG. 3. Formation of the pseudo-projection stream used for cardiorespiratory motion tracking. (**a**) One complete coverage of the 144-PE Cartesian k-space (over ~375 ms) during scanning, where the phase encodes were ordered by the discrete golden step scheme. Imaging readouts inside the navigator zone (central 10% of k_y) were used for motion tracking. (**b**) Magnitude of the inverse Fourier transform, the pseudo-projections. Imaging data acquisition covered the k-space repeatedly for the entire duration of the scan. (**c**) The first 1000 raw pseudo-projections (over ~28 s), though motion is not immediately recognizable. (**d**, **e**) After magnitude scaling (d) to reduce k_y-dependent intensity fluctuation and smoothing along time (e) to further reduce high-frequency changes, cardiac and respiratory motions are visible in the final form. The white arrows mark five cardiac cycles; the black arrows mark two respiratory cycles.

inverse of the average of the three distances was used as the sharpness (15,16). Both SAX and LAX images at end systole and end diastole were evaluated.

In addition, as a surrogate for cardiac function, endocardial and epicardial contours were manually drawn on both end-diastolic and end-systolic frames of SAX cines. The area difference (epi minus endo) measured single-slice myocardial area (mm^2). The percent area change of the endocardial contour was considered the single-slice ejection fraction. These functional measures of the GS BH and GS FB scans were compared with ECG BH using a two-tailed paired Student *t* test with modified Bonferroni correction. The threshold of significance was set at a corrected *P* value of 0.05.

RESULTS

Simulation

As seen in Figure 2, circular phantoms of diameters of 1/2, 1/4, 1/8, and 1/16 FOV retained projection appearance on pseudo-projections at up to 2, 4, 8, and 16 $\times$ Δk_y, respectively. In other words, the phantom's projection image started to vanish when the spatial period of the phase-encoding complex sinusoid approached the phantom size. Smaller objects remained visible when using higher-order phase encodes, but with the aforementioned cost of diminished signal level.

Pseudo-Projection Formation

Pseudo-projection appearance at each stage of processing is shown in Figure 3. The pseudo-projection streams generated with various navigator zone widths are compared in Figure 4, using data from an example scan. Initially, increasing navigator zone width would reveal more features of motion, but at approximately central 10% of k_y, both cardiac and respiratory motions were fully revealed. Beyond 10%, no additional information was revealed, and cardiac motion was often suppressed.

Cardiac and Respiratory Motion Tracking

For all subjects imaged, cardiac motion and respiratory motion were captured within the first five most significant eigenvectors of the pseudo-projections covariance matrix. As shown in Figure 5, the identified cardiac and respiratory eigenvectors were filtered to form the motion waveform. The correspondence between the cardiac events generated by self-gating and the reference ECG triggers was high (Figure 5c). As shown in Figure 5d, the generated respiratory motion curve closely followed the respiratory motion, including the nonperiodic deviations of the motion, as seen in the initial portion of the scan. Figure 6 shows the quantitative comparison between cardiac motion tracking and reference ECG, aggregated for all imaged subjects except one for whom the ECG data failed to record. Overall, the self-gating cardiac events were accurate to about 30 ms with respect to ECG, with the Trough being the most accurate event type.

Self-Gated Cine Quality

Motion tracking was successful in all golden step scans. Cines were composed of 25–30 cardiac phases to match the temporal resolutions of their respective reference

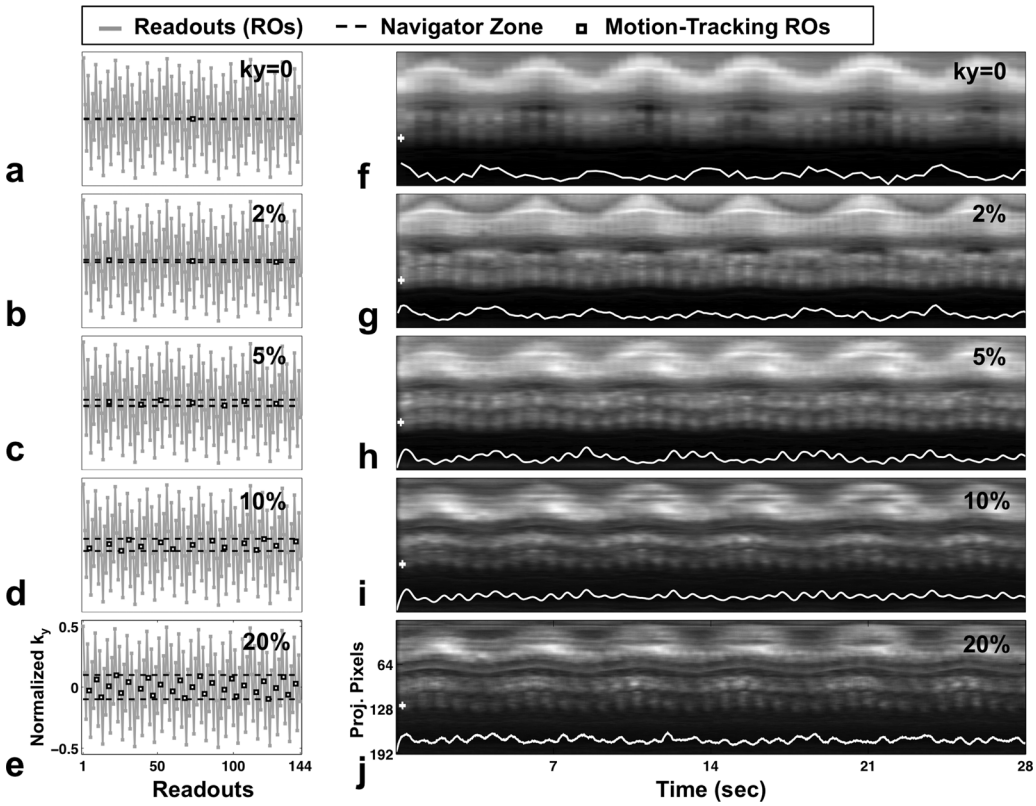

FIG. 4. Widths of the navigator zone (**a**–**e**) and its impact on the processed pseudo-projection stream (**f**–**j**) during a free-breathing cardiac scan. The intensity over time of the marked pixels is superimposed on each stream (white). The narrowest navigator zone width corresponded to the conventional projection-based motion tracking using only the $k_y = 0$ readout (a, f), which revealed respiratory motion only. As higher-k_y PEs were included, cardiac motion started to emerge (second and third rows). At a width of 10% k_y (d, i), both cardiac and respiratory motions were fully revealed. This resulted in a motion-sampling frequency of 38 Hz and was used to process all scans in this study. Beyond 10%, no additional motion information was revealed, and respiratory motion may become degraded. All data shown in this figure originated from the same duration of the same scan, as widths of the navigator zone could be freely adjusted retrospectively.

scans. A comparison of ECG BH, GS BH, and GS FB reconstructions is shown in Figure 7. Both golden step self-gated cines showed very similar image quality as the reference scans. Small features such as the papillary muscles and trabeculae carnae are clearly visualized, and nuances of motion such as the "atrial kick" can be seen in the motion profiles. However, the golden step cines, especially in LAX cines, were prone to signal inhomogeneity or loss in the regions of rapid blood flow (see Discussion). This is better visualized in Figure 8, which compares the entire cardiac cycle.

Sharpness Measurements

LV myocardial sharpness measurements of the golden step self-gated cines are compared with those of the reference cines in Figure 9. In general, the self-gated cine sharpness was similar to the references, with SAX sharpness slightly greater than LAX, and end-systole sharpness comparable to end-diastole.

Functional Measurements

As seen in Figure 10, the LV blood pool area, the LV myocardial area, and the single-slice ejection fraction as measured on the self-gating cines showed good agreement with those of the reference cines. For each functional metric, no statistically significant difference was found between the self-gated cines and the reference cines at a significance level of Bonferroni-corrected P value of 0.05.

DISCUSSION

In this study, we demonstrated the efficacy of using pseudo-projections in cardiorespiratory motion tracking. By deriving both cardiac and respiratory motions solely from imaging readouts, this technique allows for ECG-free and breath hold-free scanning without the loss of imaging efficiency typical in other techniques. The quality of the self-gated cardiac cines was similar to the ECG-gated breath-hold cines, making it possible to perform ECG-free and breath-hold free cardiac function studies.

The foremost advantage of the proposed technique is that it captures both kinds of motion with minimal prescan planning, since the optimal navigator zone width can be determined after imaging. The number of cardiac phases (consequently, temporal resolution) can also be adjusted retrospectively, while the k-space coverage in

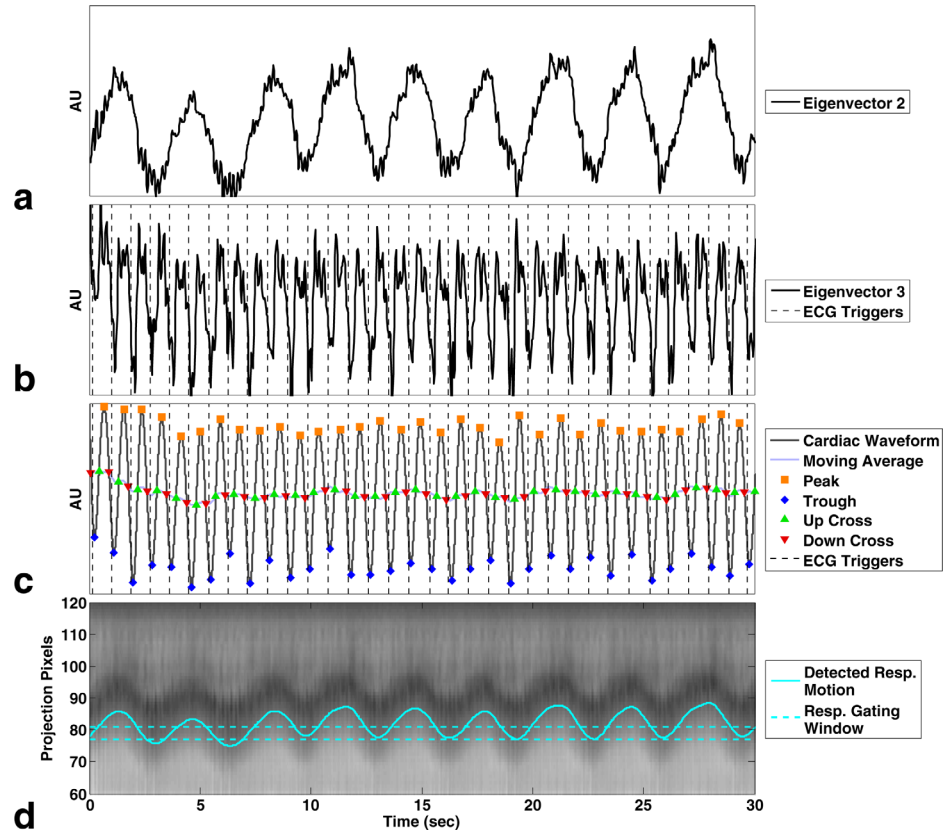

FIG. 5. Example of the PCA-based motion extraction from a free-breathing scan. In this example, the second (**a**) and third (**b**) most significant eigenvectors of the pseudo-projections covariance matrix predominantly carried respiratory and cardiac motion, respectively (the first eigenvector carried a DC signal level). The cardiac eigenvector was filtered, and a moving-average-crossing algorithm was applied to generate self-gating events (**c**). The recorded ECG-derived triggers are also shown on **b** and **c** as the timing reference. (**d**) Filtered respiratory eigenvector superimposed on the pseudo-projections showing nine cycles of respiratory motion (a respiratory-dominant coil is shown, although all coils were used in motion extraction). Also superimposed is the respiratory gating window around the most frequent position of the waveform, preliminarily accepting 30% of the data. Note that the more irregular portion of the respiratory motion was preserved (first 10 s).

each phase remains uniform. There is no need to fix the number of readouts per segment as in many previously reported self-gating techniques [eg, (11–13,15)]. The only remaining motion-related parameter to be chosen is the total scan duration per slice, which can be set to arbitrary values that can take into account respiratory rate, making the duration of cardiac function portion of the MRI study simply dependent on the number of slices to acquire. Any additional readouts will benefit all k-space regions equally.

Although we used a Fibonacci number as the number of PEs (N_{PE}) in this study, N_{PE} need not be a Fibonacci number. For any desired number of phase encode steps, the next greater Fibonacci number can be used to generate PE indices. Any indices greater than the desired N_{PE} are skipped. For example, if N_{PE} = 256, a k-space with $F_{14} = 377$ phase encodes is designed. Any indexes greater than 255 are skipped. With this approach, coverage of k_y is still pseudorandom, because just like the navigator zone, the N_{PE} k_y-space is simply a subsection of the Fibonacci k_y-space.

Pseudo-projections do have the limitation of only detecting motion along the readout direction. As such, some care has to be taken during slice localization so

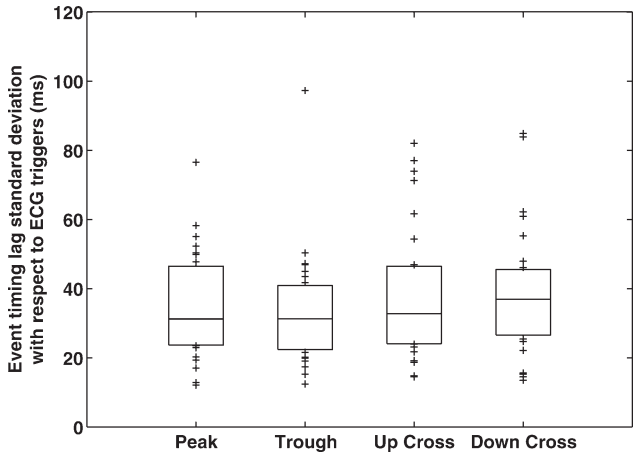

FIG. 6. Timing errors by event type of cardiac self-gating events. Each data point represents a golden step scan, marking the standard deviation of the timing differences between the automatically detected self-gating events and their corresponding ECG triggers. The lower, middle, and upper edges of each box indicate the 25th, 50th, and 75th percentiles, respectively. In self-gated reconstructions, the type with the lowest event interval variance was used to generate cardiac triggers. Troughs were the least variable and were selected for triggering in 12 out of the 16 scans.

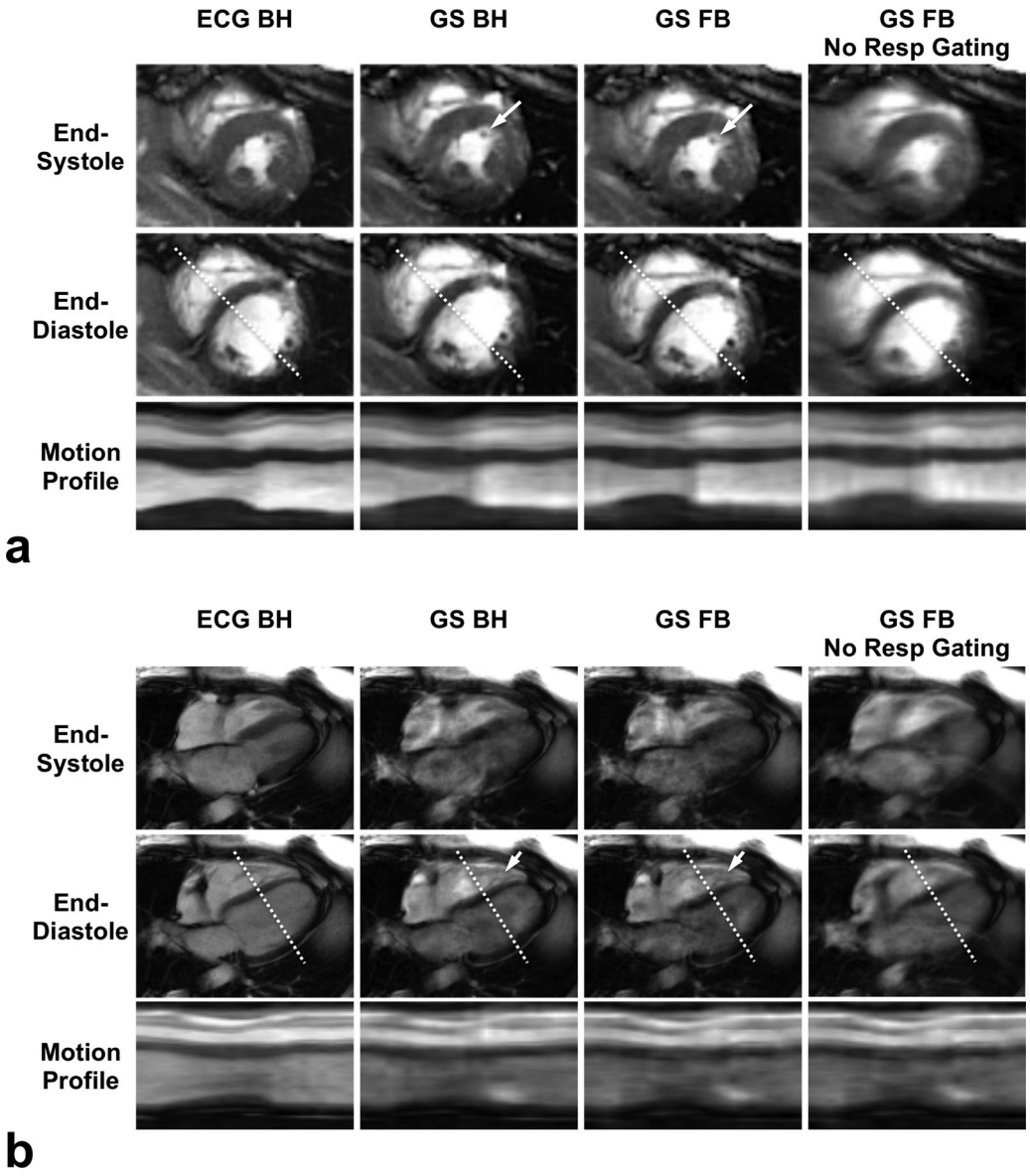

FIG. 7. End-systolic and end-diastolic frames of self-gated cines (GS BH, GS FB) compared with breath-hold ECG references (ECG BH). In both SAX (**a**) and LAX (**b**) cines, small features (white arrows) were well resolved in self-gated reconstructions. Golden step acquisitions reconstructed without respiratory gating (GS FB No Resp Gating) show the effects of motion. The motion profiles visualize the time course of intensity over a line segment of the image (dashed lines). In golden step acquisitions, however, regions of blood flow were prone to signal inhomogeneity or loss, especially in the LAX orientation. ECG BH, standard prospective ECG-gated breath-hold acquisition; GS BH, golden-step breath-hold acquisition with cardiac self-gating; GS FB, golden-step free-breathing acquisition with both cardiac and respiratory self-gating.

that significant components of motion project onto the readout direction. However, cardiac cycles can be readily detected regardless of the readout orientation due to the high signal intensity change of ventricular blood pool. As with projection-based techniques, pseudo-projections enable the gating of motion but do not provide enough information for cardiorespiratory motion to be corrected. Along the PE direction, pseudo-projections are insensitive to rigid motion and may be corrupted by nonrigid motion. Through-plane motion can be detected only if it produces enough intensity change in the imaging plane to project onto the readout direction, and still the displacement of such motion cannot be determined. These limitations would make it difficult to accurately detect respiratory motion, which is more complex and subject-dependent and has motivated many sophisticated subject-specific models [eg, three-dimensional translational (43), elliptical (44), affine (45), nonrigid (17,46)]. Even with similarity-based data sorting, projection-based gating in the current technique still assumes repeatability of respiratory motion, and one can expect more subject-dependent variability in the performance of respiratory motion tracking.

The PCA-based method that extracted the cardiac and respiratory motion waveforms from the pseudo-projection stream assumed that the two types of motion were

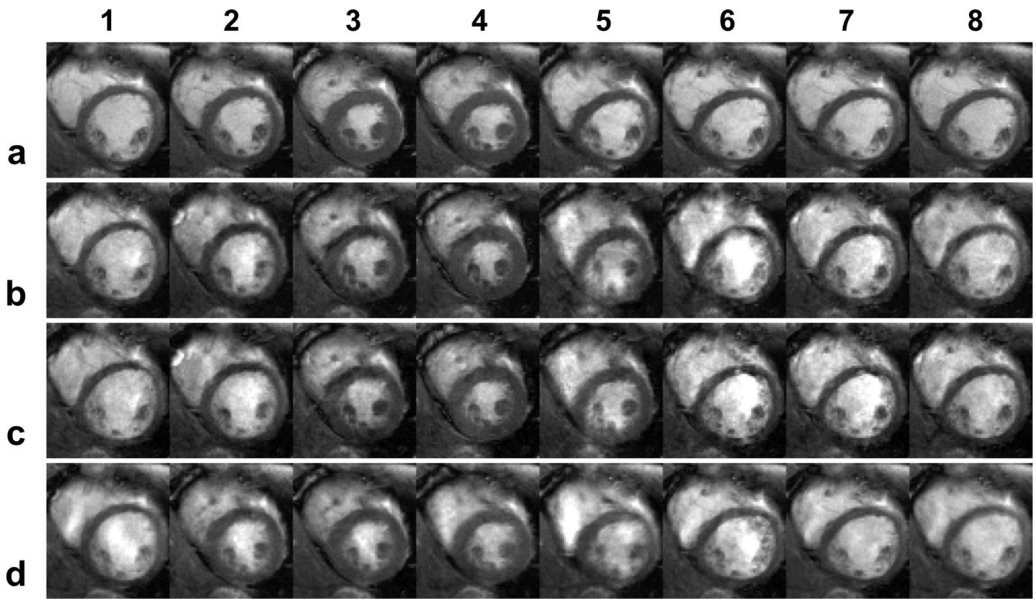

FIG. 8. Comparison of cine frames showing eddy current and flow-induced artifact during a cardiac cycle. (**a**) Reference cine (ECG BH) acquired with sequential PE, ECG gating, and breath hold. (**b**) golden-step breath-hold acquisition (GS BH) reconstructed using ECG gating and no self-gating. (**c**) the same GS BH acquisition reconstructed with cardiac self-gating. (**d**) golden-step free-breathing acquisition (GS FB) reconstructed with cardiac and respiratory self-gating. Compared with the reference, signal disturbance and smearing in and around the cardiac blood pool can be seen in all three golden step acquisitions, particularly in cardiac phases where blood flow is the highest (ie, columns 2, 5, and 6). Given that similar levels of artifact can be seen in panels b–d regardless of the motion tracking method, the artifact is most likely independent of self-gating and due to flow effects compounded by eddy currents associated with golden step PE jumps.

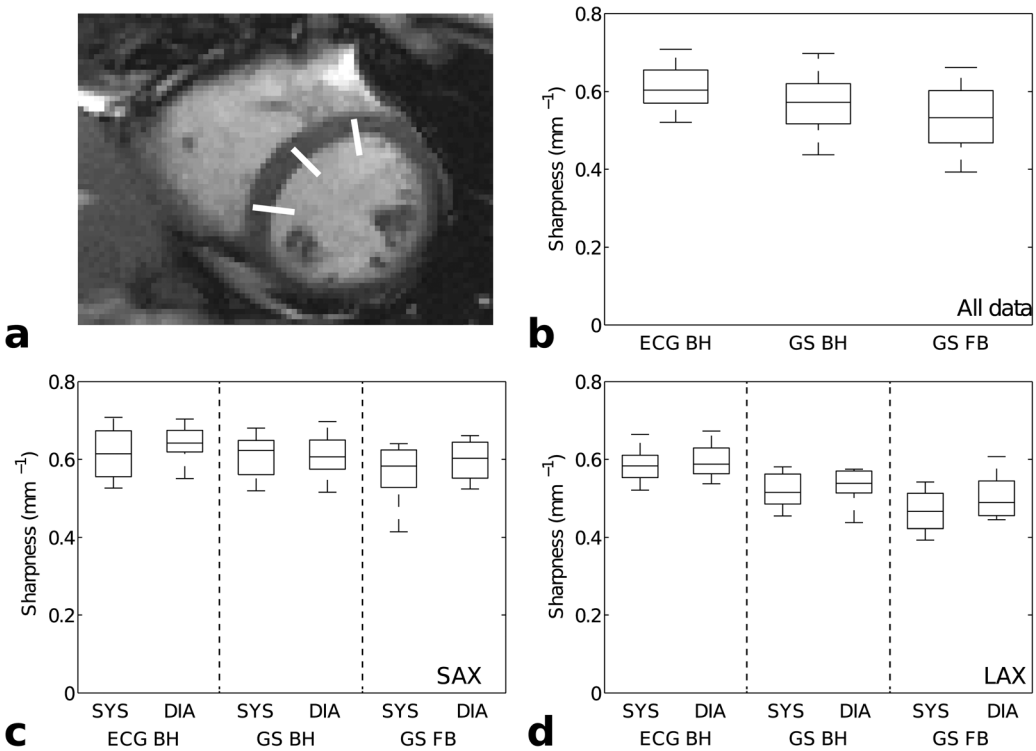

FIG. 9. Comparison of sharpness measurements from the golden-step self-gated cines (GS BH, GS FB) and those of the reference cines (ECG BH). (**a**) Example of sharpness profile placement. (**b**) All sharpness measurements made on end-systolic and end-diastolic frame from SAX and LAX slices, categorized only by scan types. (**c**, **d**) Measurements from SAX (c) and LAX (d) slices are compared and categorized by both scan type and cardiac state. The SAX sharpness measurements were slightly greater than those for LAX, and end-systolic (SYS) and end-diastolic (DIA) measurements were comparable. For all box plots, the lower, middle, and upper edge of each box indicate the 25th, 50th, and 75th percentiles, respectively, and the extremes of the whiskers cover the range of data. BH, breath-hold; FB, free breathing; GS, golden step; LAX, long axis; SAX, short axis.

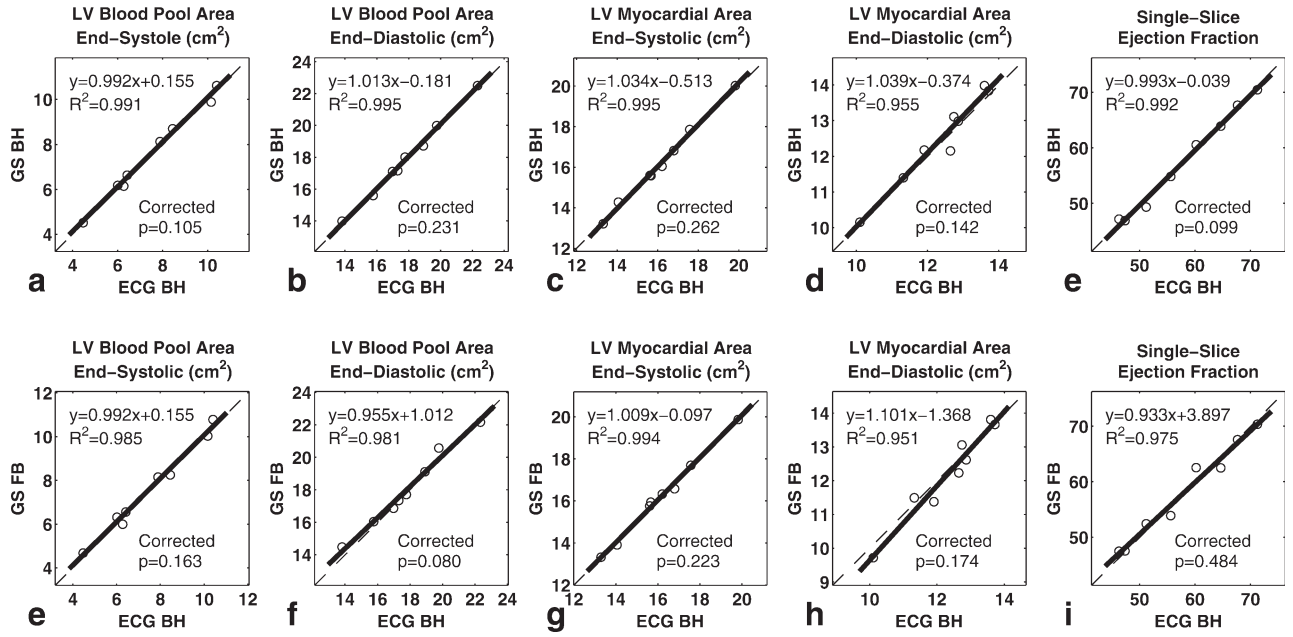

FIG. 10. Comparison of functional measurements from golden step self-gated cines (GS BH, first row; GS FB, second row) and those of the reference cines (ECG BH). Obtained from regions of interest drawn on SAX cines, LV blood pool area (**a**, **b**, **e**, **f**), LV myocardial area (**c**, **d**, **g**, **h**), and single-slice ejection fraction (**e**, **i**) of the self-gated cines showed good agreement with those of the reference cines. Linear regressions (solid black lines) are superimposed over the identity lines (dashed lines). *P* values obtained using a Bonferroni-corrected *t* test are also displayed. For each functional metric, no statistically significant difference was found between self-gated cines and reference cines at a significance level of $P = 0.05$ (Bonferroni-corrected). BH, breath-hold; FB, free breathing; GS, golden step.

sufficiently distinct from each other and could be captured in two principal components. Experimental results showed that this assumption was reasonable. As shown in Figure 7, the majority of the standard deviations of the timing lags between self-gating events and ECG triggers were within 20–50 ms, which is comparable to the duration of a k-space segment in cardiac imaging or 5% of a typical RR interval. There were extraneous frequencies on both cardiac and respiratory eigenvectors, but they were relatively mild and were effectively removed by filtering. For additional robustness, two pseudo-projection streams could be generated to separately emphasize cardiac and respiratory motions by using different navigator zones and temporal filters. PCA could then be applied to the two streams separately to target different motion frequencies.

As noted in the Results, golden step cines are sensitive to signal inhomogeneity or loss in the blood pool. The resultant artifact, sometimes referred to as the "dark flow" artifact, has a distinct appearance and is well known in bSSFP imaging. It has been attributed to a combination of flow and field inhomogeneity (47–50), both of which disturb the bSSFP steady state by introducing extraneous phase to the spins in every TR. The affected spins may lose steady state and undergo oscillation, causing signal inhomogeneity or loss. The use of golden step further introduces field inhomogeneity due to its relatively large PE stepping between consecutive readouts. Large PE jumps are known to cause additional field disturbances by inducing eddy currents in the scanner body (51). This compounds with the sustained in-plane flow to make golden step scans, particular LAX slices, vulnerable to the artifact.

As a hardware phenomenon, eddy currents are difficult to eliminate, but compensatory techniques are available to reduce their effects at run time, via PE pairing (51), doubling (52), and other arrangements (53,54). At postprocessing, the dark flow artifact can also be reduced using principles of parallel imaging (55). Careful shimming of the scanner main field and shifting the center frequency are most likely to improve image quality (47,48,50,56). Because both eddy currents and imperfect main fields can result in unwanted phase accrual on spins, improving the local main field will reduce the total phase accrual and may prevent some spins from undergoing oscillation. At the sequence level, specialized techniques such as S5FP (57) can be used to eliminate spins corrupted by phase and flow. Steady-state incoherent techniques such as spoiled gradient echo imaging (SPGR) are much less sensitive to extraneous phase, and can be used to avoid the artifact altogether, especially at higher field strengths, albeit with a very different image contrast and reduced SNR.

Parallel imaging and compressed sensing were not used in this study, so that motion tracking could be evaluated in isolation. Hence, scan durations in this study were longer than necessary in a clinical setting. Parallel imaging and sparse-recovery reconstruction techniques can be readily applied. For example, given the large amount of data acquired in the golden step scans, it would be straightforward to measure convolution weights for GRAPPA (58) and to achieve acceleration rates of 2 or 3. Free-breathing scan time could be reduced to approximately 30 s per slice at 30 ms cine temporal resolution. One can also randomly skip readouts outside the navigator zone and recover them

using GRAPPA, calibrated using the fully sampled navigator zone (which in this case must be fixed before the scan).

Although the original golden angle work was radial (33) and radial projection-based self-gating already exists (13), the current Cartesian implementation is still desirable: for sequence programming, the proposed technique is a PE reordering scheme and can be easily added onto 2D Cartesian sequences, which are widely used. For motion detection, respiratory tracking is easier with the constant viewing angle of Cartesian pseudo-projections rather than the constantly changing projection angle of radial acquisition. For image reconstruction, one simply uses the inverse Fourier transform and need not involve gradient delay correction or regridding of nonuniform k-space samples in radial imaging.

Winkelmann et al. (33) proposed a radial acquisition using a real-value golden-angle increment ($\sim$111.2°), which permitted continuous acquisition without repetition of any readout angulation. Although this study used an integer golden step, the real-valued golden step could also be used in Cartesian imaging (36): a normalized k_y-space is described by a continuous interval of -0.5 to 0.5, and the real-valued PE position therein is incremented by the golden ratio conjugate, $\Delta k = (\sqrt{5}-1)/2 \approx 0.618$, after every readout (and circularly wrapped within the interval). In the real-valued scheme, no PE position is ever repeated, and as a result no limitation exists in the image matrix size. However, because the PE position no longer falls onto the Cartesian grid, the magnitude scaling factor $c(x, k_y)$ would need to be made continuous along k_y, which can be achieved by data fitting or interpolation. Additionally, image reconstruction with real-valued PEs would require k-space regridding or a generalized inversion approach, which may be more computationally intensive and may impact image quality in technique-dependent ways, but may be more amenable to incorporation of sparse reconstruction techniques. The discrete integer golden step used in this work could take advantage of the fast Fourier transform for straightforward image reconstruction and has adequately demonstrated the motion tracking ability of near-center PEs.

CONCLUSION

The use of pseudo-projections in conjunction with golden step phase encoding was found feasible for free-breathing, non-ECG cardiac imaging. It was shown to be capable of tracking both cardiac and respiratory motions, and cardiac cine images with quality comparable to that of breath-hold scans were obtained. Despite some sensitivity to flow and eddy currents, the simplicity of acquisition makes the proposed technique a valuable tool for self-gated cardiac imaging.

REFERENCES

1. Atkinson DJ, Edelman RR. Cineangiography of the heart in a single breath hold with a segmented turboFLASH sequence. Radiology 1991;178:357–360.
2. Setser RM, Fischer SE, Lorenz CH. Quantification of left ventricular function with magnetic resonance images acquired in real time. J Magn Reson Imaging 2000;12:430–438.
3. Plein S, Smith WH, Ridgway JP, Kassner A, Beacock DJ, Bloomer TN, Sivananthan MU. Qualitative and quantitative analysis of regional left ventricular wall dynamics using real-time magnetic resonance imaging: comparison with conventional breath-hold gradient echo acquisition in volunteers and patients. J Magn Reson Imaging 2001;14:23–30.
4. Kaji S, Yang PC, Kerr AB, Tang WH, Meyer CH, Macovski A, Pauly JM, Nishimura DG, Hu BS. Rapid evaluation of left ventricular volume and mass without breath-holding using real-time interactive cardiac magnetic resonance imaging system. J Am Coll Cardiol 2001;38:527–533.
5. Rokey R, Wendt RE, Johnston DL. Monitoring of acutely ill patients during nuclear magnetic resonance imaging: use of a time-varying filter electrocardiographic gating device to reduce gradient artifacts. Magn Reson Med 1988;6:240–245.
6. Polson MJ, Barker AT, Gardiner S. The effect of rapid rise-time magnetic fields on the ECG of the rat. Clin Phys Physiol Meas 1982;3:231–234.
7. Kugel H, Bremer C, Puschel M, Fischbach R, Lenzen H, Tombach B, Van Aken H, Heindel W. Hazardous situation in the MR bore: induction in ECG leads causes fire. Eur Radiol 2003;13:690–694.
8. Lange SAM, Nguyen QNB. Cables and electrodes can burn patients during MRI. Nursing (Lond) 2006;36:18.
9. Crowe ME, Larson AC, Zhang Q, Carr J, White RD, Li D, Simonetti OP. Automated rectilinear self-gated cardiac cine imaging. Magn Reson Med 2004;52:782–788.
10. Buehrer M, Curcic J, Boesiger P, Kozerke S. Prospective self-gating for simultaneous compensation of cardiac and respiratory motion. Magn Reson Med 2008;60:683–690.
11. Larson AC, White RD, Laub G, McVeigh ER, Li D, Simonetti OP. Self-gated cardiac cine MRI. Magn Reson Med 2004;51:93–102.
12. Hiba B, Richard N, Janier M, Croisille P. Cardiac and respiratory double self-gated cine MRI in the mouse at 7 T. Magn Reson Med 2006;55:506–513.
13. Liu J, Spincemaille P, Codella NC, Nguyen TD, Prince MR, Wang Y. Respiratory and cardiac self-gated free-breathing cardiac CINE imaging with multiecho 3D hybrid radial SSFP acquisition. Magn Reson Med 2010;63:1230–1237.
14. Larson AC, Kellman P, Arai A, Hirsch GA, McVeigh E, Li D, Simonetti OP. Preliminary investigation of respiratory self-gating for free-breathing segmented cine MRI. Magn Reson Med 2005;53:159–168.
15. Kellman P, Chefd'hotel C, Lorenz CH, Mancini C, Arai AE, McVeigh ER. High spatial and temporal resolution cardiac cine MRI from retrospective reconstruction of data acquired in real time using motion correction and resorting. Magn Reson Med 2009;62:1557–1564.
16. Pipe JG. Motion correction with PROPELLER MRI: application to head motion and free-breathing cardiac imaging. Magn Reson Med 1999;42:963–969.
17. Wang CC, Huang TY. Self-gated PROPELLER-encoded cine cardiac imaging. Int J Cardiovasc Imaging 2012;28:1477–1485.
18. Stehning C, Bornert P, Nehrke K, Eggers H, Stuber M. Free-breathing whole-heart coronary MRA with 3D radial SSFP and self-navigated image reconstruction. Magn Reson Med 2005;54:476–480.
19. Lustig M, Cunningham CH, Daniyalzade E, Pauly JM. Butterfly: A Self Navigating Cartesian Trajectory. In Proceedings of the 15th Annual Meeting of ISMRM, Berlin, Germany, 2007. p. 865.
20. Spraggins TA. Wireless retrospective gating: application to cine cardiac imaging. Magn Reson Imaging 1990;8:675–681.
21. White RD, Paschal CB, Clampitt ME, Spraggins TA, Lenz GW. Electrocardiograph-independent, "wireless" cardiovascular cine MR imaging. J Magn Reson Imaging 1991;1:347–355.
22. Guo L, McVeigh ER, Lederman RJ, Derbyshire JA, Herzka DA. Dual-Projection Cardiac and Respiratory Self-Navigated Cine Imaging Using SSFP. In Proceedings of the 18th Annual Meeting of ISMRM, Stockholm, Sweden, 2010. p. 78.
23. Guo L, Segundo AJM, Derbyshire JA, Carrino JA, Herzka DA. Self-Navigated Kinematic Imaging of the Knee. In Proceedings of the 19th Annual Meeting of the ISMRM, Montreal, Quebec, Canada, 2011. p. 384.
24. Lai P, Larson AC, Park J, Carr JC, Li D. Respiratory self-gated four-dimensional coronary MR angiography: a feasibility study. Magn Reson Med 2008;59:1378–1385.
25. Lai P, Larson AC, Bi X, Jerecic R, Li D. A dual-projection respiratory self-gating technique for whole-heart coronary MRA. J Magn Reson Imaging 2008;28:612–620.
26. Jin N, Lewandowski RJ, Omary RA, Larson AC. Respiratory self-gating for free-breathing abdominal phase-contrast blood flow measurements. J Magn Reson Imaging 2009;29:860–868.
27. Hu P, Hong S, Moghari MH, Goddu B, Goepfert L, Kissinger K V, Hauser TH, Manning WJ, Nezafat R. Motion correction using coil

arrays (MOCCA) for free-breathing cardiac cine MRI. Magn Reson Med 2011;66:467–475.
28. Kadah YM, Abaza AA, Fahmy AS, Youssef AB, Heberlein K, Hu XP. Floating navigator echo (FNAV) for in-plane 2D translational motion estimation. Magn Reson Med 2004;51:403–407.
29. Mendes J, Kholmovski E, Parker DL. Rigid-body motion correction with self-navigation MRI. Magn Reson Med 2009;61:739–747.
30. Lin W, Huang F, Bornert P, Li Y, Reykowski A. Motion correction using an enhanced floating navigator and GRAPPA operations. Magn Reson Med 2010;63:339–348.
31. Mendes J, Parker DL. Intrinsic detection of motion in segmented sequences. Magn Reson Med 2011;65:1084–1089.
32. Guo L, Sayin O, Derbyshire JA, Herzka DA. Navigator-Free Self-Gated Dynamic Cine Imaging Using 2D Cartesian Golden Step Phase Encoding. In Proceedings of the 20th Annual Meeting of ISMRM, Melbourne, Victoria, Australia, 2012. p. 515.
33. Winkelmann S, Schaeffter T, Koehler T, Eggers H, Doessel O. An optimal radial profile order based on the golden ratio for time-resolved MRI. IEEE Trans Med Imaging 2007;26:68–76.
34. Ehman RL, Felmlee JP. Adaptive technique for high-definition MR imaging of moving structures. Radiology 1989;173:255–263.
35. Wang Y, Grimm RC, Felmlee JP, Riederer SJ, Ehman RL. Algorithms for extracting motion information from navigator echoes. Magn Reson Med 1996;36:117–123.
36. Derbyshire JA, Saybasili H, Guo L, Sayin O, Kellman P, Lederman RJ, Herzka DA. Golden Step Phase Encoding: Simultaneous real-time and ECG Gated-Cine Parallel MRI with Retrospective Selection of Temporal Resolution, Acceleration Rate and Acquisition Duration. In Proceedings of the 19th Annual Meeting of the ISMRM, Montreal, Quebec, Canada, 2011. p. 4364.
37. Derbyshire JA, Herzka DA, McVeigh ER, Lederman RJ. Efficient implementation of hardware-optimized gradient sequences for real-time imaging. Magn Reson Med 2010;64:1814–1820.
38. Scheffler K, Heid O, Hennig J. Magnetization Preparation During the Steady State: Fat Saturated 3D TrueFISP. In Proceedings of the 9th Annual Meeting of ISMRM, Glasgow, United Kingdom, 2001. p. 440.
39. Odille F, Uribe S, Batchelor PG, Prieto C, Schaeffter T, Atkinson D. Model-based reconstruction for cardiac cine MRI without ECG or breath holding. Magn Reson Med 2010;63:1247–1257.
40. Lu W, Nystrom MM, Parikh PJ, Fooshee DR, Hubenschmidt JP, Bradley JD, Low DA. A semi-automatic method for peak and valley detection in free-breathing respiratory waveforms. Med Phys 2006;33:3634–3636.
41. Feinstein JA, Epstein FH, Arai AE, Foo TKF, Hartley MR, Balaban RS, Wolff SD. Using cardiac phase to order reconstruction (CAPTOR): a method to improve diastolic images. J Magn Reson Imaging 1997;7:794–798.
42. Taylor AM, Jhooti P, Wiesmann F, Keegan J, Firmin DN, Pennell DJ. MR navigator-echo monitoring of temporal changes in diaphragm position: implications for MR coronary angiography. J Magn Reson Imaging 1997;7:629–636.
43. Moghari MH, Hu P, Kissinger KV, Goddu B, Goepfert L, Ngo L, Manning WJ, Nezafat R. Subject-specific estimation of respiratory navigator tracking factor for free-breathing cardiovascular MR. Magn Reson Med 2012;67:1665–1672.
44. Burger I, Meintjes EM. Elliptical subject-specific model of respiratory motion for cardiac MRI. Magn Reson Med 2013;70:722–731.
45. Leung AO, Paterson I, Thompson RB. Free-breathing cine MRI. Magn Reson Med 2008;60:709–717.
46. Hansen MS, Sørensen TS, Arai AE, Kellman P. Retrospective reconstruction of high temporal resolution cine images from real-time MRI using iterative motion correction. Magn Reson Med 2012;68:741–750.
47. Deshpande VS, Shea SM, Li D. Artifact reduction in true-FISP imaging of the coronary arteries by adjusting imaging frequency. Magn Reson Med 2003;49:803–809.
48. Li W, Storey P, Chen Q, Li BSY, Prasad P V, Edelman RR. Dark flow artifacts with steady-state free precession cine MR technique: causes and implications for cardiac MR imaging. Radiology 2004;230:569–575.
49. Bi X, Park J, Deshpande V, Simonetti O, Laub G, Li D. Reduction of flow- and eddy-currents-induced image artifacts in coronary magnetic resonance angiography using a linear centric-encoding SSFP sequence. Magn Reson Imaging 2007;25:1138–1147.
50. Saremi F, Grizzard JD, Kim RJ. Optimizing cardiac MR imaging: practical remedies for artifacts. Radiographics 2008;28:1161–1187.
51. Bieri O, Markl M, Scheffler K. Analysis and compensation of eddy currents in balanced SSFP. Magn Reson Med 2005;54:129–137.
52. Markl M, Leupold J, Bieri O, Scheffler K, Hennig J. Double average parallel steady-state free precession imaging: optimized eddy current and transient oscillation compensation. Magn Reson Med 2005;54:965–974.
53. Nielsen J-F, Nayak KS. Interleaved balanced SSFP imaging: artifact reduction using gradient waveform grouping. J Magn Reson Imaging 2009;29:745–750.
54. Fischer RF, Barmet C, Rudin M, Boesiger P, Pruessmann KP, Kozerke S. Monitoring and compensating phase imperfections in cine balanced steady-state free precession. Magn Reson Med 2013;70:1567–1579.
55. Winkelmann R, Börnert P, Dössel O. Ghost artifact removal using a parallel imaging approach. Magn Reson Med 2005;54:1002–1009.
56. Amano Y, Nozaki A, Takahama K, Kumazaki T. Reduction in flow artifacts by using interleaved data acquisition in segmented balanced steady-state free precession cardiac MRI. Comput Med Imaging Graph 2005;29:441–445.
57. Derbyshire JA, Guttman MA, Lederman RJ, McVeigh ER. Reduction of Flow Artifacts in Balanced SSFP Imaging Using S5FP. In Proceedings of the 16th Annual Meeting of ISMRM, Montreal, Quebec, Canada, 2008. p. 211.
58. Griswold MA, Jakob PM, Heidemann RM, Nittka M, Jellus V, Wang J, Kiefer B, Haase A. Generalized autocalibrating partially parallel acquisitions (GRAPPA). Magn Reson Med 2002;47:1202–1210.